J. Space Weather Space Clim. 2025, **15**, 38

https://doi.org/10.1051/swsc/2025032

JSWSC

Available online at:
www.swsc-journal.org

RESEARCH ARTICLE OPEN ACCESS

Transition from westward to eastward tilts of equatorial plasma bubbles observed by an all-sky airglow imager

Xingyan Song[1], Jiahao Zhong[1,2,*], Yongqiang Hao[1], Tao Bai[3], Xin Wan[1,2], Fuqing Huang[4], Qiaoling Li[5], Jing Zhao[1], Hao Han[1], Jiawen Chen[1], and Jiuhou Lei[4]

[1] Planetary Environmental and Astrobiological Research Laboratory (PEARL), School of Atmospheric Sciences, Sun Yat-sen University, 519080 Zhuhai, PR China
[2] Key Laboratory of Tropical Atmosphere-Ocean System, Ministry of Education, 519080 Zhuhai, PR China
[3] Unit 94188 of Chinese People's Liberation Army, 710000 Xi'an, PR China
[4] CAS Key Laboratory of Geospace Environment, School of Earth and Space Sciences, University of Science and Technology of China, 230026 Hefei, PR China
[5] China University of Petroleum-Beijing at Karamay, 834000 Xinjiang, PR China

Received 14 March 2025 / Accepted 8 July 2025

Abstract – Equatorial plasma bubbles (EPBs) typically form after sunset at the bottom of the F layer in the equatorial region and then grow upward and elongate along magnetic flux tubes. According to optical observations, in many cases, the poleward ends of EPBs tilt westward with respect to the magnetic north, but in a few cases, eastward tilts are observed. In this work, the EPB tilt directions, drift velocities, and morphology are investigated from an all-sky airglow imager over South China during the geomagnetically quiet night of April 3, 2022. During this event, the poleward ends of the EPBs in the off-equatorial region initially tilted westward after sunset (20:04–23:27 LT), but gradually turned to tilt eastward around and after midnight (23:27–03:38 LT). Successive airglow images revealed different groups of EPBs with westward tilts, westward-eastward tilts, and eastward tilts throughout a single night. The changes in morphology, tilt angles, and drift velocities of EPBs are analyzed according to the airglow images. The tilt angles ranged from −12° to 25°, which were calculated by Principal Component Analysis (PCA) through Singular Value Decomposition (SVD). The westward-to-eastward tilt direction changed in less than 17 min, and the eastward tilt of the EPBs lasted 4 h. When the EPBs drifted eastward over the observation region, the ionogram displayed distinct spread F signatures, and satellite signals manifested significant scintillation phenomena. The drift velocities of the EPBs at relatively high latitudes clearly increased and were greater than those at lower latitudes when the EPBs turned to tilt eastward at approximately 23:27 LT (15:53 UT), with a velocity differential of 20 m/s. The changes in tilt direction may result from latitudinal variations in ion drift velocities, which might be related to the latitudinal/altitudinal variations in F-region Pedersen conductivity and the presence of greater zonal winds or electric fields along the geomagnetic field line.

Keywords: Equatorial plasma bubble / Tilt direction / Airglow image / Ion drift velocity / Zonal wind velocity

1 Introduction

Equatorial plasma bubbles (EPBs) are plasma density depletion structures in the ionospheric F region at equatorial and low latitudes, typically triggered by Rayleigh-Taylor instability and lifted by the pre-reversal enhancement (PRE) of the eastward electric field after sunset. Near sunset, as the solar radiation source diminishes, the ionospheric E region undergoes significant reduction due to rapid electron-ion recombination, while the F region maintains substantial electron density, as the lower ion-neutral collision frequencies at F region altitude result in slower recombination rates (Ossakow et al., 1979; Das et al., 2022). This fundamental difference in the temporal evolution of the E and F regions during sunset significantly influences the subsequent development of ionospheric irregularities. The combination of a steep electron density gradient at the bottom of the ionosphere and the vertical uplift of the equatorial F layer driven by PRE creates favorable conditions for an increased Rayleigh-Taylor instability growth rate, which is conducive to the occurrence of EPB (Dungey, 1956; Sultan, 1996).

*Corresponding author: zhongjh55@mail.sysu.edu.cn

After being generated by the Rayleigh-Taylor instability, EPB moves upward from the bottom of the F layer and elongates along magnetic flux tubes to reach off-equatorial latitudes (Weber et al., 1978; Otsuka et al., 2002; Yokoyama et al., 2014).

The plasma depletion structure within EPB generally presents sharp plasma density gradients, which cause significant disturbances when radio waves pass through it, manifesting as signal scintillation, and in severe cases, even causes complete signal loss, leading to reduced positioning accuracy and compromised navigation system reliability (Xiong et al., 2018b). A comprehensive understanding of EPB evolution processes is therefore essential for advancing predictive models and developing mitigation strategies for satellite-based technologies and infrastructure. EPBs can be observed by many instruments at low latitudes in different forms, including plume-like structures in backscatter echoes from incoherent radars (Woodman & La Hoz, 1976; Tsunoda & White, 1981), strong scattered echoes from coherent scatter radar (Miller et al., 2010; Chen et al., 2023), diffuse echoes of spread F from digisondes (Booker & Wells, 1938a; Wang et al., 2015), dark stripes on airglow images in optical observations from ground-based all-sky imagers (ASIs) or space-based ultraviolet (UV) measurements (Cai et al., 2020), total electron density (TEC) depletion measured by Global Navigation Satellite System (GNSS) measurements (Magdaleno et al., 2017; Vital et al., 2024) and in situ plasma density depletions from Low-Earth Orbiting (LEO) satellites (Zakharenkova et al., 2023). In practical studies, multiple instruments and data are combined to analyze the characteristics of EPB (Aa et al., 2020; Calabia et al., 2024).

The tilt direction of EPB, a distinctive morphological feature observed in airglow images, exhibits a strong correlation with key ionospheric parameters, particularly the zonal neutral wind patterns and Pedersen conductivity distribution (Huba et al., 2009; Richmond et al., 2015). This relationship provides critical insights into the complex interplay between the background ionosphere-thermosphere system and plasma irregularity evolution.

To date, many westward tilt structures at the poleward ends of EPBs with respect to the magnetic meridian have been recorded on airglow images by ASIs (e.g., Kelley et al., 2003; Otsuka et al., 2004; Wu et al., 2021), the Global Ultraviolet Imager (GUVI) on the Thermosphere Ionosphere Mesosphere Energetics and Dynamics (TIMED) satellite (e.g., Kelley et al., 2003; Kil et al., 2004), and the Global-scale Observations of the Limb and Disk (GOLD) imager (e.g., Aa et al., 2020; Cai et al., 2020). Apart from westward tilts, a few observations and statistical analyses of EPBs also reveal eastward tilts, but their occurrence rate is significantly lower than that of westward tilts (Sinha & Raizada, 2000; Sun et al., 2016). A statistical analysis of EPBs from an ASI network in China revealed that eastward tilts are rare and occur mainly in September and October over South China (Sun et al., 2016); however, in March and April, there are few eastward tilt angle records. According to airglow observations, EPBs can develop various characteristic shapes, including westward-tilted structures whose northern and southern poleward ends both tilt westward (reverse C-shape), field-aligned forms extending along the magnetic meridian (I-shape), eastward-tilted structures whose northern and southern poleward ends both tilt eastward (C-shape), and more complex patterns that feature an eastward-tilted northern end, a westward-tilted southern end, and a centrally aligned or slightly westward-tilted section (S-shape). Karan et al. (2023) reported three EPBs with a reversed "C" shape, an "I" shape, and a "C" shape simultaneously in a small longitudinal region of ~10° after sunset. The change from a westward tilt to an eastward tilt has also been shown in Chapagain et al. (2012b). The authors reported an EPB event in which bubbles close to the equator moved westward while bubble structures at higher latitudes moved eastward at 16°S during the night of April 4–5, 1997. In addition, the evolution of EPBs from an "I" shape to an "S" shape has also been reported, with the northern end of the EPBs (structures above 19°N) tilted from westward to eastward after midnight (Wu et al., 2017; Sun et al., 2021). In addition, previous optical observations of eastward-tilted EPBs have been predominantly limited to the period before 02:30 local time (LT), leaving several critical questions unanswered. First, the existence and characteristics of EPBs after 02:30 LT require systematic investigation. Second, the latitudinal dependence of tilt angle variations and associated drift velocities remains poorly characterized. Third, the fundamental nature of the ionospheric conditions that facilitate eastward EPB tilt formation constitutes a significant knowledge gap in our understanding of post-midnight ionospheric irregularity dynamics.

Several factors can influence changes in the tilt direction of EPBs, including zonal wind, Pedersen conductivity, and the ion drag force (Sinha & Raizada, 2000; Kil et al., 2009). In the literature, the westward tilts have been explained by multiple mechanisms, mainly the following:

1. An eastward zonal wind can polarize EPBs at higher altitudes and reduce the eastward drift velocity of the apex of the bubbles, resulting in westward tilts (Woodman & La Hoz, 1976). Kil et al. (2009) used an illustration to explain this mechanism.
2. In a numerical simulation, Zalesak et al. (1982) showed that the bubbles drifted faster at the altitude where the Pedersen conductivity was greatest. Above that altitude, the bubbles drifted more slowly and tilted westward. The Pedersen conductivity Σ_F^P has an impact on the vertical polarization electric field engendered by the dynamo effect of zonal neutral winds. Hence, it influences the $E \times B$ zonal drift induced by the polarization electric field (Heelis, 2004).
3. Anderson & Mendillo (1983) suggested that westward tilts were associated with decreasing eastward plasma drifts at higher altitudes, which were caused by latitudinal variations in zonal winds, although Pedersen conductivity increased at higher altitudes in these conditions. This is because the dynamo polarization electric field maps along the entire magnetic field line. As a result, when zonal wind decreases with latitude, the eastward drift velocity will decline with altitudes near the equator and cause westward tilts (Heelis, 2004; Arruda et al., 2006).
4. High plasma density in the EIA crest region results in a greater ion drag force and slower plasma drift. When the EPB extends into the EIA crest, the poleward end of the EPB tilts westward. In addition, many studies have shown that the variation in plasma drift velocity is similar to that in zonal wind velocity at different altitudes/ latitudes, which is caused by the electric field driven by zonal wind (Rishbeth, 1971; Richmond et al., 1992; Chapagain et al., 2012a). A stronger eastward zonal wind at lower

altitudes/latitudes can cause poleward ends of EPBs to tilt westward at higher altitudes and off- equatorial latitudes (Martinis et al., 2003; Huba et al., 2009).

Similarly, the eastward tilts can be related to a stronger westward plasma drift at lower altitudes/latitudes caused by zonal winds (Huba et al., 2009). Since the EPBs rise to higher altitudes from the bottom of the ionosphere and elongate along the magnetic flux tubes from the equatorial region to the off-equatorial regions, the latitudinal variation in the drift is related to its altitudinal variation in the equatorial region. Some observations and simulations have also shown a stronger eastward zonal plasma drift in off-equatorial regions or a stronger westward zonal plasma drift in equatorial regions, which can be related to the E-region electric dynamo (Aggson et al., 1987; Karan et al., 2023; Martinis et al., 2003). Above the F peak height, the F-layer dynamo drives the eastward plasma drift, whereas below the F peak height, the E-layer dynamo drives the westward plasma drift or a smaller eastward plasma drift (Haerendel et al., 1992). This shear of plasma drift velocity can cause the eastward tilt.

Thus, EPB tilt directions are related to variations in plasma drift at different altitudes/latitudes, which can be affected by zonal winds, Pedersen conductivity variations, the ion drag force, and the shear of the E-F layer dynamo. The physical explanation of the variations in the tilt directions is complex and not well understood. The westward tilt is related mainly to the ion drag force, which decreases the plasma drift velocity. The causes of the eastward tilt remain uncertain. Besides, although eastward-tilted EPBs were identified in previous airglow observations, possible subsequent EPB occurrences at later local times and their potential tilt variations have not been consistently addressed in previous research. In addition, the duration of the change in tilt direction and the variation of tilt angles during this process have rarely been documented.

In this paper, we report a special EPB event during the night of April 3, 2022, with interesting features: EPBs in different groups continuously tilt from westward to eastward. We focus on changes in the tilt direction, tracking the changes in tilt angle and in EPB drift velocities. We also examine the ion drift velocity and zonal wind velocity from the Ionospheric Connection Explorer (ICON) satellite to investigate potential correlations between these parameters and the observed changes in tilt. In the following sections, we introduce the data and methods used in this work in Section 2, and the observation results are displayed in Section 3. In Section 4, a discussion to explain the changes in the spread F in ionograms and why the EPBs tended to tilt eastward during this event is provided. Finally, a summary is given in Section 5.

2 Data and methods

The airglow images were obtained from the ASI located at the Zhuhai Campus of Sun Yat-sen University (113.58°E, 22.35°N, dip latitude 13.19°N). These data are publicly available via the Zenodo database at https://doi.org/10.5281/zenodo.11180799. The ASI is a Keo Scientific Sentry 4 Monochromatic Imager. It is composed of a Mamiya RZ67 37 mm/f4.5 medium-format achromatic fisheye lens with a 180° Field Of View (FOV), a series of optical lenses, a filter wheel with six positions, and a Charge-Coupled Device (CCD) detector. The physical dimensions of the CCD array are 27.6 × 27.6 mm, consisting of 2048 × 2048 pixels with a pixel depth of 16 bits. The camera system was thermoelectrically cooled to −80 °C (dark current < 0.5 electrons/pixel/s). The ASI is equipped with a filter at a center wavelength of 630.0 nm with a bandwidth of 2.0 nm. The 630.0 nm airglow emissions were recorded by the CCD with an integration time of 60 s.

The airglow images underwent the following processing steps before use. The first step is to correct the center and azimuth of the airglow images. The zenith is set as the center of the image, and the image is rotated around the zenith until the line from the zenith to the Polaris points north. The second step involves projecting the airglow images onto geographic coordinates. Assuming an airglow height of 250 km, each data grid point is projected onto geographic latitude and longitude coordinates based on the distance and azimuth from the zenith. Then, the airglow images are filtered by the median within 40 × 40 pixels to mitigate the effect of starlight. After that, the airglow images are cropped centered on the zenith within a 400-pixel radius. The radius range of the valid data is approximately 400 km (approximately 120° FOV).

We apply an algorithm to extract the boundaries of the depletions. First, we remove the average of the airglow images within a 30-minute window centered on each airglow image. Figure 1a presents an airglow image with its average background removed, captured at 01:01 LT on April 4, 2022. Secondly, the airglow image was transformed into binary representations as shown in Figure 1b. In a binary image, each pixel was assigned 0 (rendered as white) or 1 (rendered as black) based on the intensity levels in the original grayscale airglow image. MATLAB (Matrix Laboratory)'s imbinarize function, using Otsu's method (Otsu, 1979), was utilized to automatically determine the optimal threshold for separating EPB structures from the background. Thirdly, morphological erosion and dilation operations were applied to the images as shown in Figure 1c, effectively isolating the EPB structure from the background. The erosion step employed a disk-shaped structuring element with a radius of 2–4 pixels, removing small-scale noise and separating the EPB structures from the background by thinning the EPB structures. This was followed by dilation with a larger disk (radius 4–8 pixels) to restore the EPB boundaries while suppressing background artifacts. The combined operations effectively isolated the EPB structures from the cluttered background. Then, in Figure 1d, small connected regions are removed to eliminate the background while preserving the EPB structures. This was achieved by detecting and removing connected components smaller than the minimum size of the EPB structures. The holes within the EPB structures arose from variations in the internal structure of the EPB as well as noise introduced during the median filtering process to remove stars and subtract the average background. These holes were filled to enhance the visual clarity of the images and to make the EPB structures more distinct, thereby facilitating subsequent edge extraction.

Next, an edge detection function is applied to accurately delineate the edges of the EPB structures, as shown in Figure 1f. The tilt direction of the EPBs is obtained through principal component analysis (PCA) (Greenacre et al., 2022). Unlike linear regression (Zou et al., 2003), which minimizes the sum of the squared distances from the data points to the fitted line along

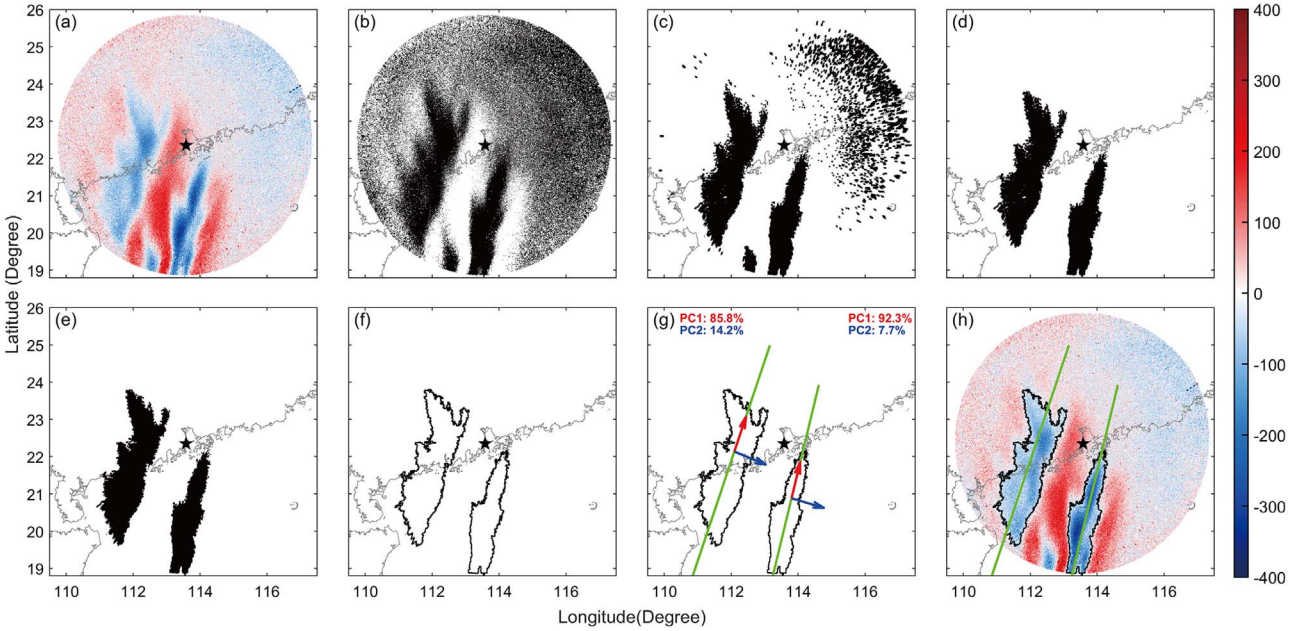

Figure 1. Process of extracting the edges and tilt directions of EPBs, using the airglow image captured at 17:26 UT on April 3, 2022 (01:01 LT on April 4) as an example. (a) Airglow image mapped to geographical coordinates. The gray line is the coastline. The black star marks the location of the all-sky imager at Zhuhai. (b) Binarized airglow image. (c) Binarized image after erosion and dilation. (d) Image after removing small connected regions. (e) Image after filling holes in connected regions. (f) Extracted edges of connected regions. (g) Principal Component Analysis (PCA) is performed on the edges of EPBs. The red arrow indicates the first principal component (PC1) direction, and the blue arrow indicates the second principal component (PC2) direction. The green lines represent the tilt directions of EPBs following the PC1 directions. The percentages at the top of the image represent the variance contributions of the first and second principal components of the two EPBs. (h) The edges and tilt directions of the EPBs are represented by the black dots and green lines on the airglow image.

the *y*-axis (the *y*-axis corresponds to the latitude in the airglow image), PCA determines the line based on the direction of maximum variance in the data (Pearson, 1901), which essentially minimizes the perpendicular distances from the data points to the fitted line. PCA ensures that the fitted line captures the overall spread and orientation of the EPB data points more accurately compared to linear regression in this work. Singular Value Decomposition (SVD) is a mathematical method that can be employed to determine the optimal fitting line direction in PCA (Greenacre et al., 2022). The eigenvector corresponding to the largest eigenvalue of SVD is the first principal component of PCA. Before using the SVD method, the coordinate matrix corresponding to the edges of EPBs was first centered by subtracting the mean value from the coordinate matrix. Based on the centered data, SVD was carried out to identify a set of orthogonal vectors that maximize the extension of the EPB in a specific direction with the largest corresponding variance, and this direction is the first principal component (PC1) direction. Figure 1g shows the PC1 direction with red arrows and green lines. The second principal component (PC2) is orthogonal to PC1. The percentages at the top represent the percentages of the total variance explained by PC1 and PC2, respectively. In this EPB event, the variance percentages explained by PC1 range from 79% to 96%, and the lines along the PC1 directions define the tilt directions of EPBs in this study.

We use data recorded by Digisonde, which allows us to detect ionospheric plasma bubbles by monitoring the well-known Range and Frequency Spread F (RSF and FSF) phenomena in ionograms (Booker & Wells, 1938b; King, 1970). For this work, ionograms were recorded at intervals of 10 min by the digisonde at the same site as the ASI. The digisonde employs radio waves ranging from 6 to 15 MHz from 15:00 to 20:00 Universal Time (UT) on April 3, 2022. An echo intensity (signal-to-noise ratio, SNR) of less than 40 dB is not used. The analysis of the echoes is focused on the evolution of spread F, which is caused by ionospheric irregularities.

To examine whether the occurrence characteristics of EPB events were influenced by geomagnetic activity, we analyzed key solar and geomagnetic indices from April 2 to 4, 2022, obtained from the OMNIWeb database (https://omniweb.gsfc.nasa.gov/). The SYMmetric Horizontal component (SYM-H) index, derived from the horizontal component of the geomagnetic field measured at ground-based observatories, was used to identify the strength and duration of geomagnetic storms. The 10.7-cm solar radio Flux (F10.7) index, measuring solar radio emission at 10.7 cm, was adopted to reflect the intensity of solar activity. The planetary K-index (Kp), calculated based on data from 13 global geomagnetic observatories, was used to describe the overall level of geomagnetic activity, ranging from 0 to 9 and quantifying global geomagnetic disturbance levels, which are based on 3-hourly measurements of geomagnetic disturbances. The Auroral Electrojet (AE) index, derived from high-latitude geomagnetic observations, was employed to characterize the intensity of substorms and reflect auroral electrojet dynamics. These indices collectively help to quantify global geomagnetic disturbance levels and auroral electrojet dynamics, which may modulate low-latitude ionospheric instability.

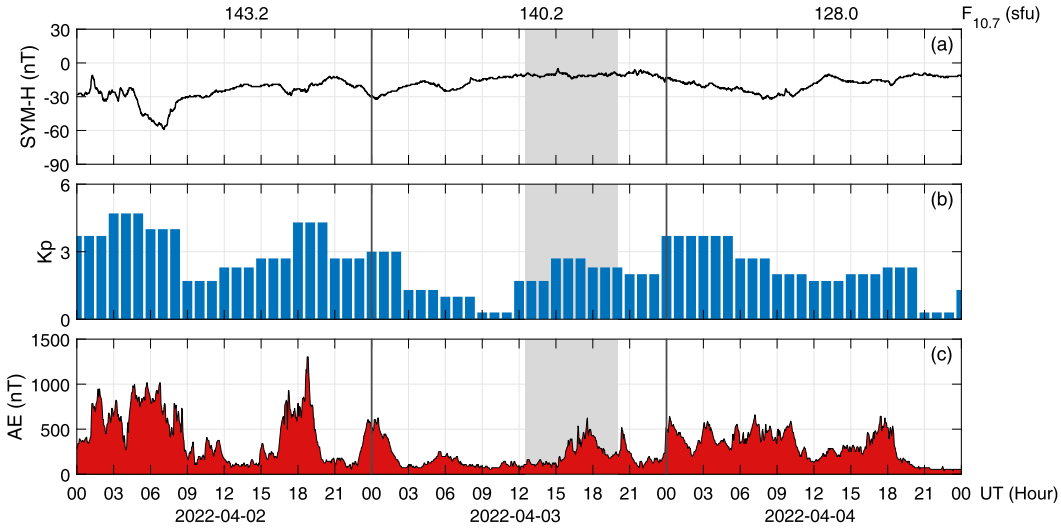

Figure 2. Solar and geomagnetic activity indices from April 2–4, 2022. The gray-shaded region marks the EPB observation from 12:30 to 20:04 UT (20:04–03:38 LT) during the night of April 3. (a) SYM-H index and $F_{10.7}$ index at the top of the panel; (b) Kp index; (c) AE index. These indices can be accessed in the GSFC/SPDF OMNIWeb database (https://omniweb.gsfc.nasa.gov/).

The amplitude Scintillation index (S4 index), a pivotal metric for quantifying ionospheric scintillation, is defined as the ratio of the standard deviation to the mean of satellite signal intensity. It effectively captures the amplitude fluctuations induced by spatial inhomogeneities in ionospheric electron density. In this study, a Septentrio PolaRx5S Ionospheric Scintillation Monitoring Receiver (ISMR) was deployed in Zhuhai. This receiver is capable of recording multi-frequency, multi-GNSS signals with a temporal resolution of 1 s for carrier phase, pseudo-range, and carrier-to-noise ratio measurements. The receiver generates the S4 index at 60-second intervals, which effectively facilitates the analysis of the impact of EPB events on satellite signal propagation. Typically, the S4 index ranges from 0 to 1. A higher S4 index indicates more pronounced fluctuations in signal strength and more intense signal scintillation.

The plasma eastward drift and zonal wind velocities measured by ICON are also analyzed. The ICON mission was launched on October 11, 2019, with a 27° inclination and 575–610 km near-circular orbit (Immel et al., 2018). The ion drift measurements were conducted in situ by an ion velocity meter (IVM) (Heelis et al., 2017), and the wind measurements were made by the Michelson Interferometer for Global High-resolution Thermospheric Imaging (MIGHTI) instrument (Englert et al., 2017). The ion drift velocity and zonal wind velocity were extracted at 105°–125°E longitude along the satellite trajectory. MIGHTI provides zonal wind velocities from 90 to 300 km, and we calculate the average zonal wind velocity at altitudes of 230–270 km.

3 Results

3.1 Solar and geomagnetic conditions

Figure 2 illustrates the solar and geomagnetic indices during April 2–4, 2022. The EPB event shown in this work was observed from 12:30 to 20:04 UT (20:04–03:38 LT) during the night of April 3, 2022, denoted by the gray-shaded region in Figure 2. Solar activity remained moderate from April 2 to April 4 (F10.7 = 143.2, 140.2, and 128.0 sfu, respectively). At 7:05 UT on April 2, the SYM-H index reached a minimum of −59 nanoTesla (nT), and the Kp index peaked at 4.7, indicating a moderate magnetic storm. In addition, the AE index exceeded 800 nT, indicating a severe geomagnetic substorm. Compared with April 2, the geomagnetic activity was quieter during the night of April 3. Although the minimum SYM-H index reached −32 nT at 0 UT on April 3, it increased to approximately −11 nT during the EPB event (gray-shaded period), with the Kp index remaining below 3, indicating quiet geomagnetic conditions. The AE index reached 500 nT during the EPB event on April 3, reflecting a weak geomagnetic substorm. On April 4, SYM-H reached a minimum of −32 nT at 08:36 UT, and Kp reached a maximum of 4 between 0 and 5 UT, accompanied by several weak geomagnetic substorms. In short, during the period when EPBs were observed by ASI in this event, the geomagnetic activity was relatively quiet overall. However, within the gray-shaded region, the AE index increased to 500 nT during the 15–18 UT interval, suggesting possible localized enhancements in magnetic activity in the polar regions.

3.2 Latitudinal extension, morphology, and tilt directions of EPBs

EPBs were observed by the ASI at Zhuhai station (113.58°E, 22.35°N) during 20:04–03:38 LT (12:30–20:04 UT) of April 3–4, 2022, with LT = UT + longitude/15. EPBs are divided into four groups according to their time sequence. The longitude between the EPB groups is approximately 5°. The distance between adjacent EPBs and the width of EPBs is approximately 1–2° at longitudes.

Figure 3 shows four groups of EPBs. Each group consists of eight consecutive subfigures. For instance, the subgraph labeled "(G1a)" corresponds to subgraph "a" of the first group. The black edges represent the outlines of EPBs, and the straight lines

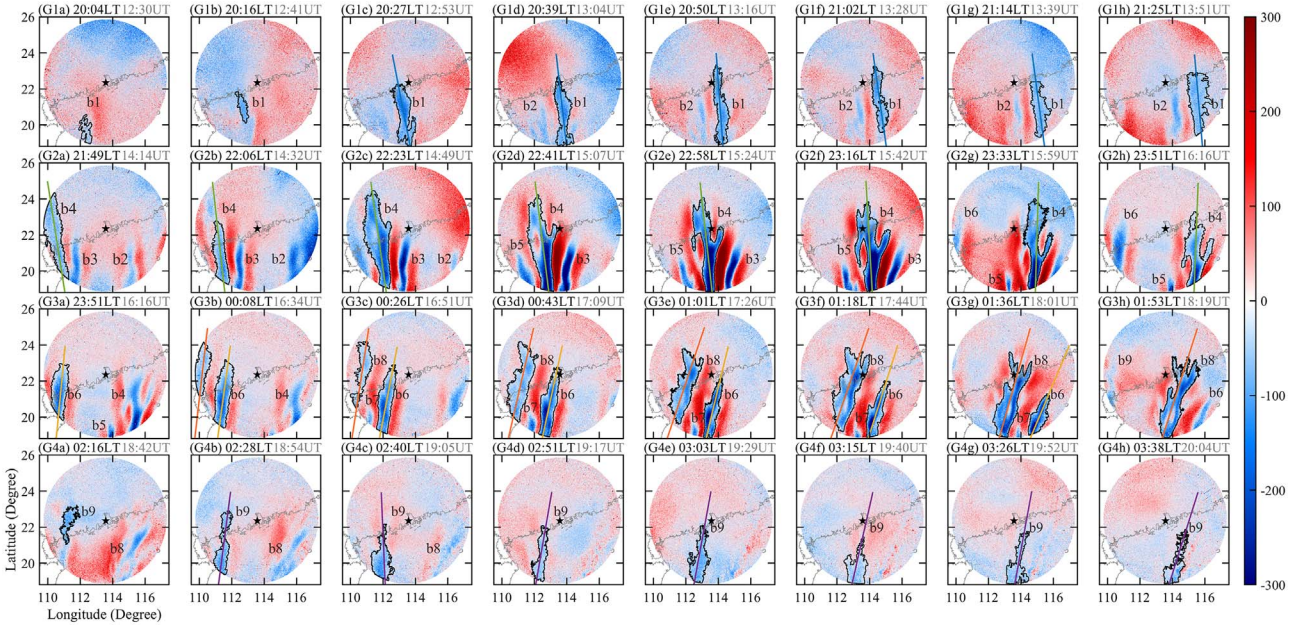

Figure 3. Airglow images during 20:04–03:38 LT (from 12:30 to 20:04 UT on April 3) during the night of April 3, 2022, in geographic coordinates. The black star denotes the location of the all-sky airglow imager at Zhuhai, and the gray line represents the coastline. The values represent the airglow intensity relative to the background, and the blue stripes with negative values are regarded as EPBs. The black edges outline the EPBs. The straight lines along the stripes represent the tilt directions of the EPB poleward ends (Fig. 4).

represent the tilt direction of the EPBs. The procedure for extracting the edges and tilt directions of EPBs is described in Section 2. The value of "b1" in G1g of Figure 3 is similar to that of the northeast region, so we cut the edges at 22.3°N during image processing. Note that the tilt lines are not marked in Figures 3(G1a), 3(G1b), or 3(G4a) because of the incomplete boundaries of the EPBs.

The first group of EPBs (G1a–G1h in Fig. 3) is set after sunset (~20:00–21:30 LT). Since the values represent the plasma density relative to the background density, blue strips with negative values are regarded as EPBs, in which the plasma density is much lower than the ambient density. The orientations of the EPBs are marked by straight lines to represent the tilt directions. Note that the main EPBs in this work are selected with a large extension and a clear structure, while "b2", "b3", "b5", and "b7" are not considered due to their small sizes. Within the visible region of the airglow image, the magnetic declination is at approximately −3°, so that the magnetic meridian lines are nearly parallel to the geographic meridian lines in the airglow images. Two stripes like EPBs can be observed in group one and are marked by "b1" and "b2". "b1" and "b2" were nearly parallel. "b1" came into the field of view earlier and extended to higher latitudes (23°N), and the depletion of "b1" was greater. Both "b1" and "b2" were slightly tilted westward during this period.

The second group of EPBs, marked by "b3", "b4", and "b5" (G2a–G2h in Fig. 3), is set before midnight (~21:50–23:50 LT). "b4" extended further than "b3" and "b5", reaching nearly 25°N. The shape of "b4" was different from that of the others. During the evolution of "b4", a hole formed in the middle region, and the southwestern part of the hole structure showed a fracture tendency, possibly related to internal EPB plasma turbulence (Xiong et al., 2018a). Three bifurcations subsequently occurred in the northern part, tilting westward, meridional, and eastward. Besides, an independent bifurcation grew on the east of "b4". The eastern part of "b4" has an "S" shaped structure (similar to the "S" shape shown by Wu et al., 2017) if we consider the eastern bifurcations at the poleward end as a "C" shape and the eastern part of the hole as a reversed "C" shape. These morphological and structural changes may be related to polarized electric fields and secondary instabilities within the bubble (Carrasco et al., 2020). According to the tilt direction marked by tilt lines in Figure 3, "b4" tilted westward before 23:16 LT and eastward after 23:33 LT. This change in the EPB tilt direction occurred in a short time, less than 17 minutes. "b3" and "b5" tilted eastward and westward, respectively. "b3" and "b5" maintained stripe-like structures, while "b4" generated bifurcations. When "b4" tilted from westward to eastward, the westward tilt angle of "b5" decreased, and the eastward tilt angle of "b3" increased.

The third group of EPBs (G3a–G3h in Fig. 3), marked by "b6", "b7" and "b8", is set at around and after midnight (~23:50–01:50 LT). "b7" showed a short portion in the airglow images, while "b6" and "b8" extended to 23°N and 24°N, respectively. "b6" maintained a stripe-like structure, while "b8" generated several bifurcations, similar to "b4". A hole gradually formed at approximately 20.5°N in "b8", and some bifurcations grew in the west and north. This group of EPBs all tilted eastward, as captured by the airglow images.

The fourth group of EPBs (G4a–G4h in Fig. 3) is set after midnight (~02:20–03:40 LT), named "b9". Since the background plasma density is low after midnight, the difference between the plasma depletion and the background plasma density is small, so the EPB is not well defined, as shown in the airglow images. "b9" was almost stripe-like, and it tilted eastward during this period. Bifurcation also occurred at

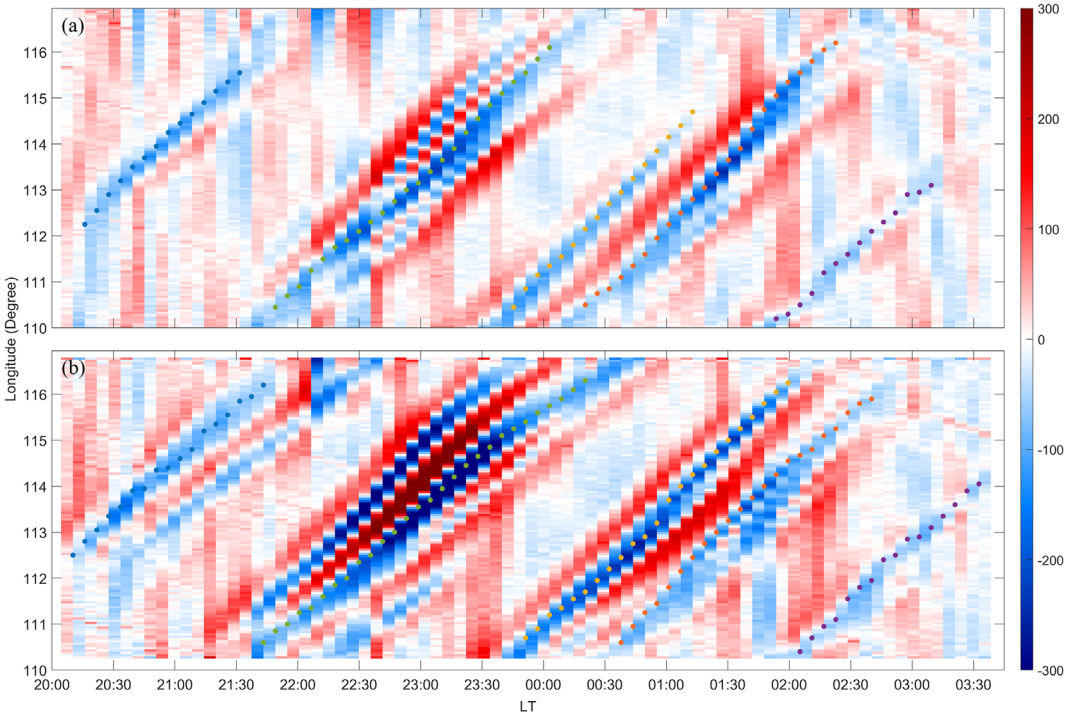

Figure 4. Keograms of the airglow values extracted at 22°N (a) and 20.5°N (b), respectively, from 20:04 to 03:38 LT during the night of April 3, 2022 (12:30–20:04 UT on April 3). The colored dots indicate the longitude position of the minimum value of each EPB structure marked by colored lines in Figure 3.

approximately 20.5°N and tilted westward. The eastward tilt angle of "b9" was less than that of "b6" and "b8". In addition, "b9" extended to 23.5°N and gradually shrank southward.

In summary, with respect to latitudinal extension, the EPBs attained their maximum northern latitudes within the range of approximately 21.5° to 25°N during this event. In terms of morphology, most EPBs were stripe-like, except for "b4" and "b8", which produced several bifurcations. For the tilt directions, the EPBs tilted westward between 20:00 and 23:16 LT, as indicated by the airglow images. At midnight, the EPBs exhibited a special change in the tilt direction. The EPBs tilted westward before 23:16 LT and turned to tilt eastward after 23:33 LT, as observed by ASI. After that, all the EPBs captured by the ASI tilted eastward. Clear airglow images continuously revealed morphological changes in the different EPB groups over the course of the night on April 3, 2022.

Figure 4 presents two keograms illustrating EPB features at 22°N and 20.5°N latitudes, respectively. The colored dots indicate the longitudinal position of the minimum value of each EPB structure marked by colored lines in Figure 3. The time interval between consecutive data points is approximately 350 s. The drift velocities of EPBs were determined by calculating the longitudinal displacement between successive images and dividing it by the time interval (EPB drift velocities = (difference in longitudes) × cos(Latitude) × 111/time interval). We applied a five-point sliding average to the velocity data, the results of which are displayed in Figure 5b.

To clarify the changes in the tilt directions of the EPBs, Figure 5a shows the changes in the tilt angles of the main EPBs over time, including "b1", "b4", "b6", "b8", and "b9". Tilt angles are calculated by the angles between the straight lines along the EPBs and the meridian line, and the eastward tilt angle is positive. Note that the geomagnetic declination in the view of the airglow images was approximately −3°. Therefore, the geographic meridian lines were nearly parallel to the magnetic meridian lines in the region of this work. Overall, the tilt angles of the EPBs ranged from −12° (westward) to 25° (eastward). "b1" tilted approximately −12° to −5° after sunset and was nearly aligned with the magnetic meridian. The tilt angle of "b4" changed gradually from −10° to 3° before midnight. "b6" tilted from 6° to 25° around and after midnight. "b8" tilted from 7° to 19° around and after midnight. "b9" was the last detected EPB, and it tilted at approximately 10°. The second data point of "b9" in Figure 5b corresponds to the tilt direction indicated by the straight line in Figure 3(G4c). Compared with adjacent airglow images, the southern part of the straight line exhibits an excessive eastward shift, resulting in significant deviation from the actual tilt direction. Besides, the Milky Way entered the field of view of the airglow images from the southeast at 02:51 LT, and approached the vicinity of "b9" by 03:38 LT. When extracting the edge of "b9" from the last image in Figure 3, the presence of the Milky Way introduced interference, leading to an increased error in the determination of the tilt angle of "b9" at 03:38 LT.

Figure 5b shows the eastward drift velocities of the main EPBs at 22°N (solid-colored lines) and 20.5°N (dashed lines) mentioned above. The black curve represents the zonal wind velocity calculated by the Horizontal Wind Model 14 (HWM14) at the ASI station (Drob et al., 2015). In Figure 5b, the drift velocity of the EPBs decreased from 87 to 55 m/s after

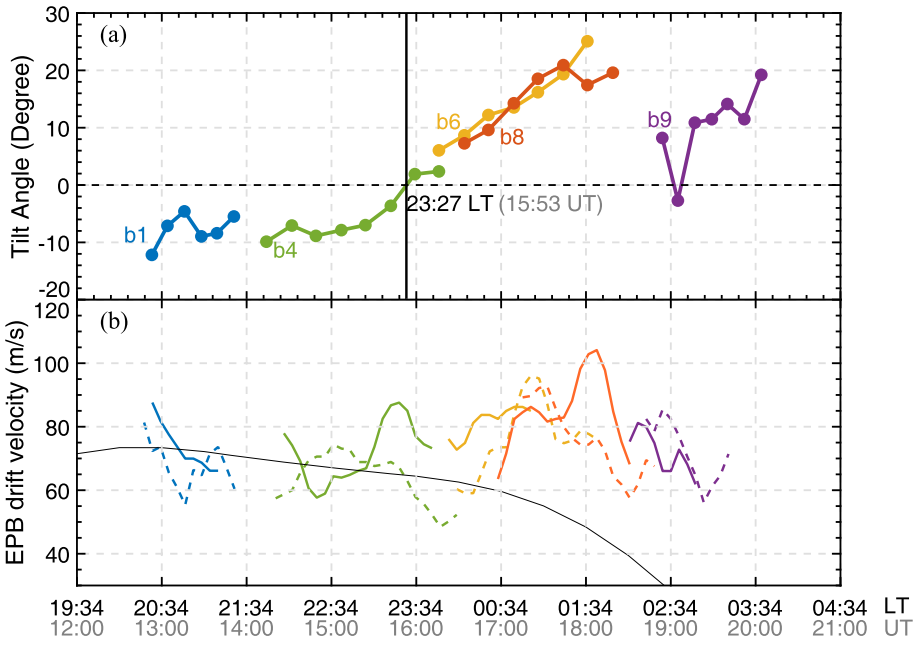

Figure 5. Variation in the tilt angles and drift velocities of the EPBs during the night of April 3, 2022 (eastward tilt is positive). (a) The values represent the tilt angles of the tilt lines marked in Figure 3 with respect to the meridian lines. The different colors of the lines in this figure correspond to the colors of the tilt lines in Figure 3. The vertical black line marks the time (23:27 LT, 15:53 UT on April 3, 2022) when the tilt directions of the EPBs changed from westward to eastward. (b) Variations in the EPB drift velocity and zonal wind velocity calculated via HWM14. The solid-colored lines represent the drift velocity of EPBs at 22°N. Dashed lines represent the drift velocity of EPBs at 20.5°N. The black curve is the zonal wind velocity calculated by HWM14 at Zhuhai station.

sunset, and at approximately 22:34 LT, the drift velocity increased significantly from 60 to 87 m/s at 22°N, whereas it decreased from 74 to 48 m/s at 20.5°N. EPB drift velocities at higher latitude (22°N) turned to be faster than those at lower latitude (20.5°N). Then, the EPBs gradually tilted eastward at 23:24 LT, with a velocity differential of 20 m/s between the higher and lower latitudes. When the EPBs tilted eastward between 23:24 and 02:00 LT, the drift velocities of "b6" and "b8" increased before 01:00 LT and decreased after that. Note that the velocities of "b8" at 22°N increased sharply around 01:34 LT due to the southward movement of the EPB, while points are not from the same part of "b9", leading to a large deviation from the real situation. During 02:00–03:00 LT, "b9" decreased. The tilt angle of "b9" was measured until 03:38 LT, while the velocity was only recorded until 03:00 LT. This temporal discrepancy arises because, subsequent to midnight, the background electron density diminishes, consequently making "b9" less visible within the keogram. Overall, the drift velocities of the EPBs at relatively high latitudes clearly increased and were greater than those at lower latitudes when the EPBs turned to tilt eastward.

As shown by the vertical black line in Figure 5, the tilt directions of the main EPBs changed from westward to eastward at approximately 23:27 LT (15:53 UT). EPBs changed their tilt directions in continuous observations during one night, and the duration of this change was less than 17 min, as seen from the airglow images. In previous studies, Chapagain et al. (2012b) reported a similar event in which the EPBs tilted from westward to eastward, but the situation of the EPBs that may have occurred behind the event has not been reported. In our work, the EPBs continued to tilt eastward and lasted until 03:38 LT. The long-lasting eastward tilt of different groups of EPBs during one night suggests that ionosphere elements such as zonal winds and plasma drift may have changed in favor of the eastward tilt and may have lasted for a period of time.

3.3 Effects of EPBs with different tilt directions on radio waves

Figure 6 shows the ionograms from the digisonde at Zhuhai station between 22:34 and 03:34 LT (15:00 and 20:00 UT) during the night of April 3, 2022. The digisonde was developed by the Ionosphere Laboratory of Wuhan University, and the color bar represents the signal-to-noise ratio (SNR) in decibels (dB) (Yao et al., 2012). Since the digisonde was under testing on the observation day, there was a lack of data before 22:30 LT. To enhance the clarity and focus of the image, the SNR data from 0 to 200 km altitude were not included in the ionograms.

In ionograms, Range Spread F (RSF) is characterized by multiple echoes appearing at various heights corresponding to the same frequency. Moreover, Frequency Spread F (FSF) is marked by echoes occurring at the same virtual height across a range of frequencies in the vicinity of the F2 peak (Bowman, 1991; Woodman, 2009). According to Figure 6, the RSFs with dispersion echoes ranging from 300 to 400 km existed from 22:34 to 23:14 LT (Figs. 6a–6c), when the EPBs tilted westward. At approximately 23:34 LT (G2g in Fig. 3), the EPBs had just changed their tilt direction to eastward, and the SNR

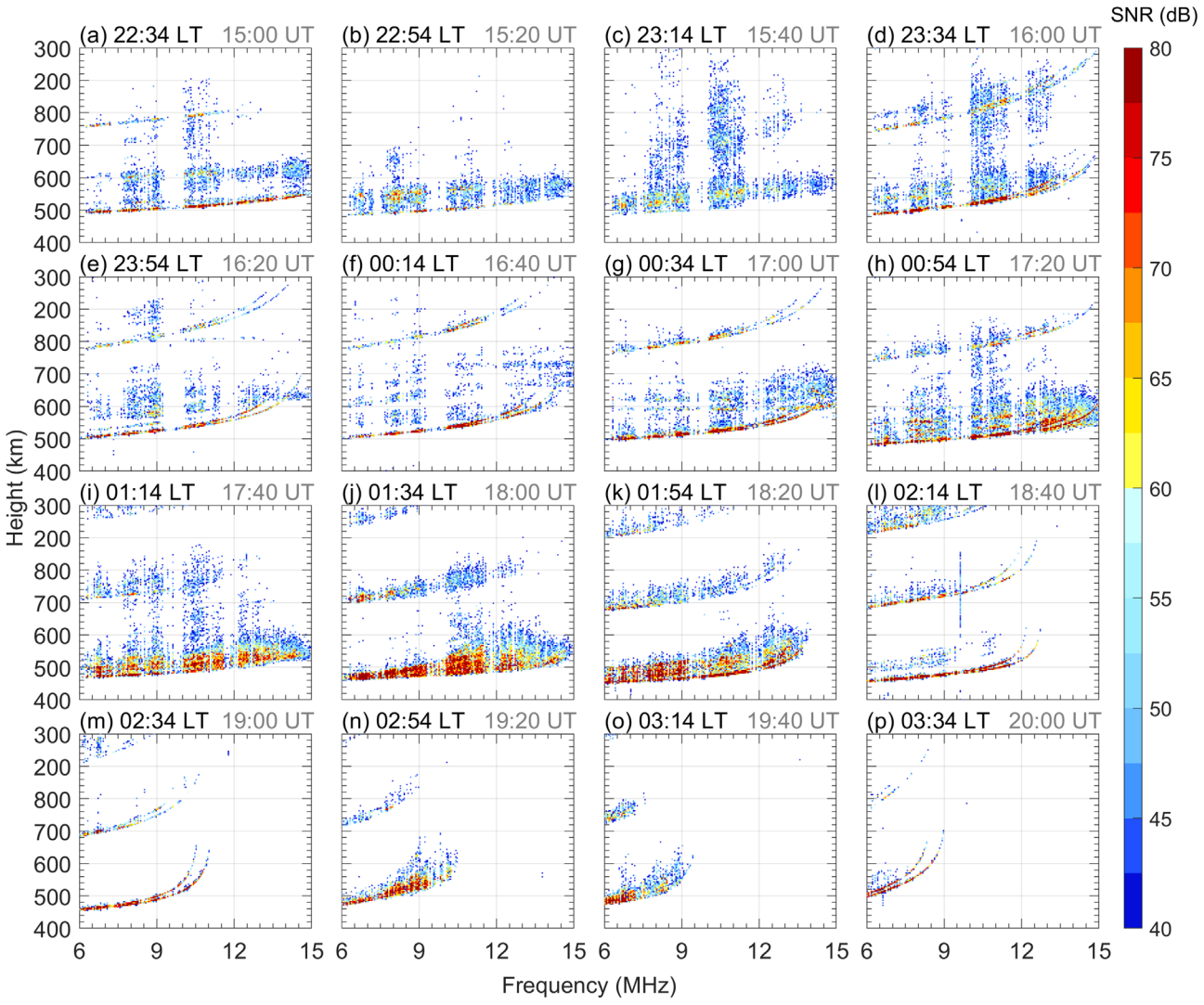

Figure 6. Ionograms observed by the digisonde at Zhuhai between 22:34 and 03:34 LT (15:00 and 20:00 UT) during the night of April 3, 2022. The time interval is 20 minutes.

at 300 km exhibited slight enhancement. The echoes around 600 km altitude are secondary echoes of those initially observed at 300–400 km. This occurs because the pulse waves emitted by Digisonde are first reflected by the ionosphere to the ground, then reflected back to the ionosphere, and finally reflected again to the receiver of the Digisonde. Similarly, echoes around 800 km are tertiary echoes. Given that multiple echoes are significantly affected by the propagation path and are thus less reliable, we focus on the variations of the primary echoes near 300–400 km. From 23:54 to 00:14 LT (Figs. 6e–6f), there was no EPB in the airglow images above Zhuhai, and the RSF still existed but was much weaker. These weaker diffuse echoes can be differentiated from those present when EPBs are above Zhuhai. During 00:34–01:54 LT (Figs. 6g–6k), "b8" tilted eastward, and the northern part of "b8" drifted over the Digisonde. The RSF was enhanced, and the echo intensity was much stronger than before. In Figure 6j, the spread F is manifested as FSF. After that, the RSF receded and disappeared at 02:14–02:34 LT (Figs. 6l–6m). Finally, FSF reoccurred at 02:54–03:14 LT (Figs. 6n–6o), when the eastward-tilted "b9" passed over Zhuhai.

Overall, the EPBs caused RSF and FSF when they passed over Zhuhai, and the eastward-tilted EPBs that occurred after midnight were associated with strong echo intensity.

In this study, EPBs were found to induce not only the equatorial spread F phenomenon in ionograms but also scintillation in satellite signals traversing the affected regions. Figure 7 illustrates the perturbation of the S4 index of the satellite signal between the Zhuhai receiver and six BeiDou geostationary satellites.

As shown in Figure 7, the irregular electron density distribution caused by EPBs leads to significant signal scintillation. By correlating the positions of EPBs in the airglow images, it is clear that the signal disturbances depicted in Figure 7 are closely linked to the passage of EPBs through the Ionospheric Pierce Points (IPPs). A detailed comparison of correlative changes in the S4 index and airglow depletion is shown by Han et al. (2024). Specifically, EPBs "b1" and "b2" induced the signal

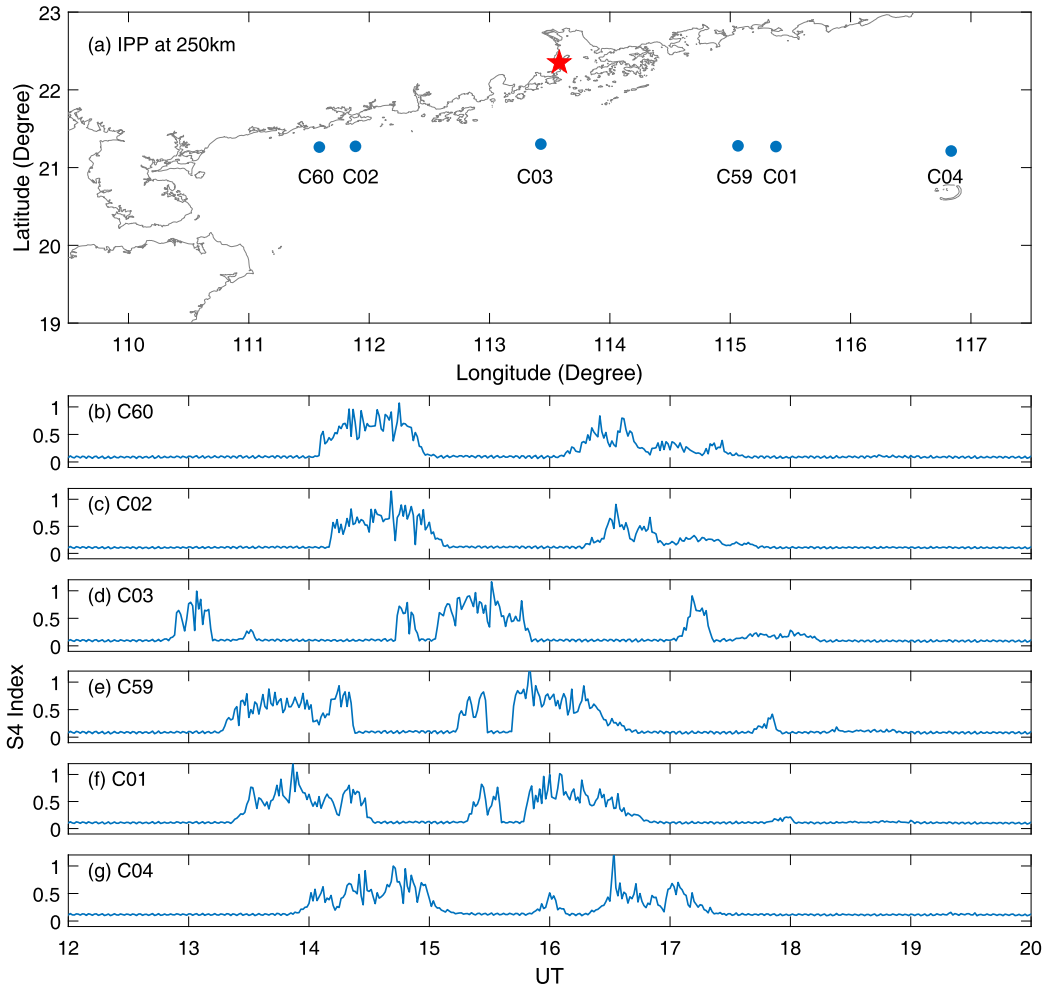

Figure 7. Variations of the S4 index of satellite signals between the Zhuhai receiver and six BeiDou GEO satellites from 12 to 20 UT on April 3 (from 19:34 LT on April 3 to 03:34 LT on April 4, 2022). (a) The red star indicates the location of the ground-based GNSS receiver in Zhuhai. The blue dots represent the ionospheric pierce points at 250 km altitude for the six GEO satellites. (b)–(g) Variations of the S4 index for satellite signals.

disruptions shown on the left side of Figures 7d–7g between 13:00 and 15:00 UT (20:34–22:34 Zhuhai LT) on April 3, 2022. EPBs "b3" and "b4" triggered disturbances in Figures 7b–7g from 14:00 to 17:00 UT (21:34–00:34 LT). Moreover, "b6" and "b8" led to disturbances in Figures 7b–7f between 16:20 and 18:00 UT (23:54–01:34 LT). The IPP of satellite C03 is uniquely located at the center of the airglow images and is far from the IPPs of other satellites. Taking advantage of this distinct configuration, we compared the start times of its S4 index disturbances with the movement of EPBs in the airglow images. The results show that the S4 disturbance around 12:50 UT happened when "b1" (G1c in Fig. 3) passed over the C03 IPP. Similarly, the disturbances at 13:25 UT, 14:40 UT, 15:05 UT, and 17:05 UT are related to the passages of "b2" (G1f in Fig. 3), "b3" (G2c in Fig. 3), "b4" (G2d in Fig. 3), and "b6" (G3d in Fig. 3) respectively. Notably, "b9" did not cause any signal disturbances. This is presumably due to the extremely low electron density in the ionosphere during nighttime, making the electron density gradients insufficient to induce signal scintillation.

3.4 Ion drift velocity and zonal wind velocity

Figure 8 displays the variation in ion drift velocity with latitude, classified by local time where the data were recorded in one-hour intervals from 20:00 to 4:00 LT. The ion drift velocities in 40 days centered on April 3 (blue dots) are used to represent the climatological variation and are compared with the situation on April 3 (red dots). As shown in Figures 8a–8c, the ion drift velocities were oriented eastward, and the velocity amplitudes were similar at latitudes of 16°–26°N. At approximately 23 LT on April 3, as shown in Figure 8d, the eastward velocity component increased at 20°–24°N, resulting in a greater eastward velocity component at relatively higher latitudes. After that, this ion drift velocity pattern was maintained from 00 to 03 LT on April 4. Similarly, the drift velocity of the EPBs in this work increased significantly at 22°N, while it decreased at 20.5°N at approximately 23 LT (Fig. 5b). After the EPBs turned to tilt eastward from 23:50 to 01:00 LT during the night of April 3, the average drift velocity of the EPBs increased. Note that the ion drift velocities on April 3 (red dots)

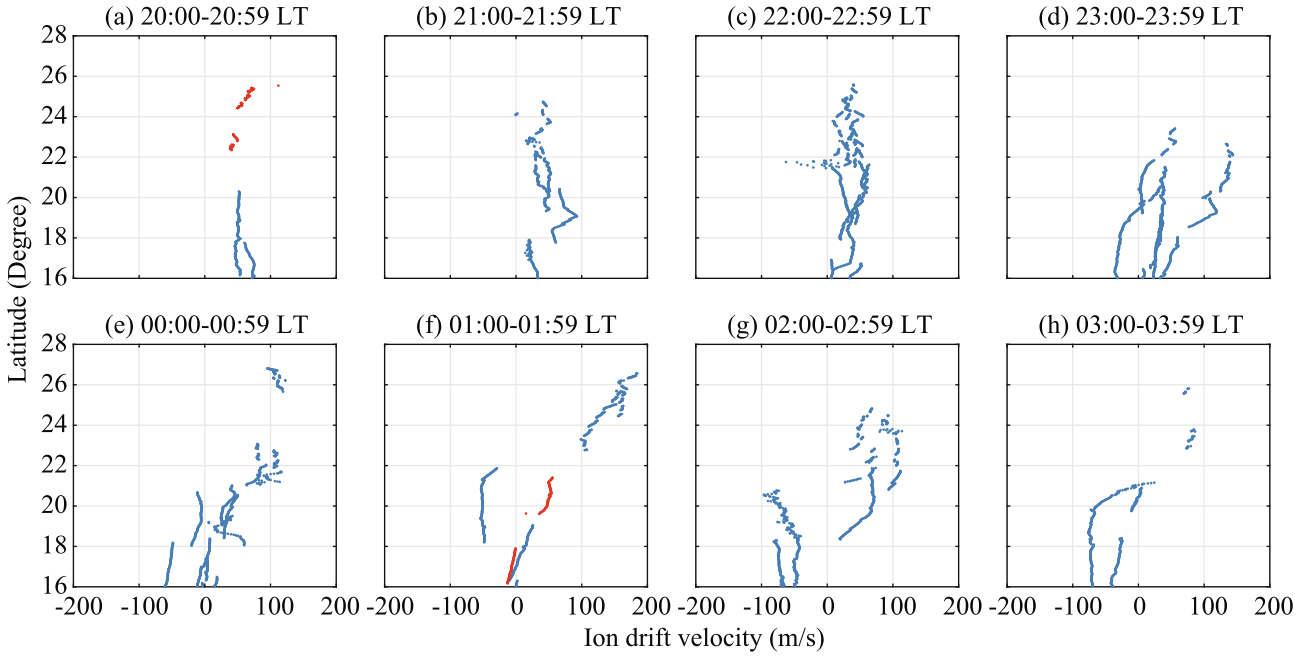

Figure 8. Ion drift velocities at longitudes of 105°–125°E measured by IVM from ICON (eastward is positive). The blue dots represent the ion drift velocities detected from March 14 to April 23, 2022 (40 days centered on April 3). The ion drift velocity data during the night of April 3 are marked by red dots.

generally followed the 40-day climatological variations (blue dots).

Figure 9 shows the variations in the average zonal wind velocities from 230 to 270 km altitude detected in the same area as the ion drift velocities. Overall, the eastward zonal wind velocities ranged from 0 to 120 m/s and slightly decreased with increasing latitude. The zonal wind latitudinal variation pattern almost did not change during the night. The zonal wind velocities on April 3 (red dots) generally followed the 40-day climatological variations (blue dots).

4 Discussions

In the EPB event that occurred during the night of April 3, 2022, the EPB moved from west to east. When passing over Zhuhai, satellite signals showed significant disturbances in the ionospheric scintillation index, and the occurrence time of the S4 index disturbance was basically consistent with the time when the EPB passed through the geographic location of the IPP. In addition, when the EPB passed over the digisonde, a remarkable spread F phenomenon appeared in ionograms. However, from 23:54 to 00:14 LT, although no EPB was observed in the airglow images, the RSF still existed but was much weaker. The different responses to the EPB could be associated with the different sensitivities of the irregularity scale sizes between the airglow imager and digisonde. At this time, the ionosphere above Zhuhai might not have recovered to a stable state, and there existed a weak depletion region above Zhuhai from 23:51 to 00:08 LT. Also, small perturbations may not be visible on airglow images due to the imager's sensitivity limitations. As a result, ionograms display weaker diffuse echoes.

In addition, the SNR increased significantly during 01:14–01:54 LT and 02:54–03:14 LT, although the cause of this enhancement remains unclear. The enhancement could potentially be attributed to changes in the spatial distribution of ionospheric electron density irregularities during the evolution of EPBs. Such variations may plausibly affect the propagation trajectories of radio waves, reflection efficiency, and phase delay characteristics. However, the Digisonde measures vertical ionospheric variations above a fixed location, while the EPB is a three-dimensional structure moving eastward. This makes it challenging to determine changes in ionospheric reflection and scattering properties during the EPB evolution. More data are needed to clarify the potential relationship between EPB evolution and modifications in ionospheric reflection properties.

The tilt angle of the EPBs exhibited a notable range, from −12° (westward) to 25° (eastward). During this EPB event, the EPBs mainly tilted westward before midnight and turned to tilt eastward at approximately 23:27 LT. After the change in the tilt direction, all the EPBs captured by the ASI tilted eastward for a long time (23:33–03:38 LT) at 109°–118°E. In terms of the EPB zonal drift, the drift velocity varied from 55 to 87 m/s, with two minimums near 21:30 and 00:00 LT and two maximums at 23:00 and 01:00 LT. When the EPBs turned to tilt eastward, the drift velocities were faster at higher latitudes (22°N). To elaborate, the poleward end of the EPB drifted faster and resulted in the eastward tilt. The drift speed at different latitudes is influenced by a multitude of factors.

A change in the tilt direction from westward to eastward is an infrequent phenomenon in the development of EPB. Some ionospheric disturbances caused by solar and geomagnetic activities may result in abnormal changes in zonal winds and electric fields, and these changes can be related to the changes in tilt directions. During the ASI observation period of this

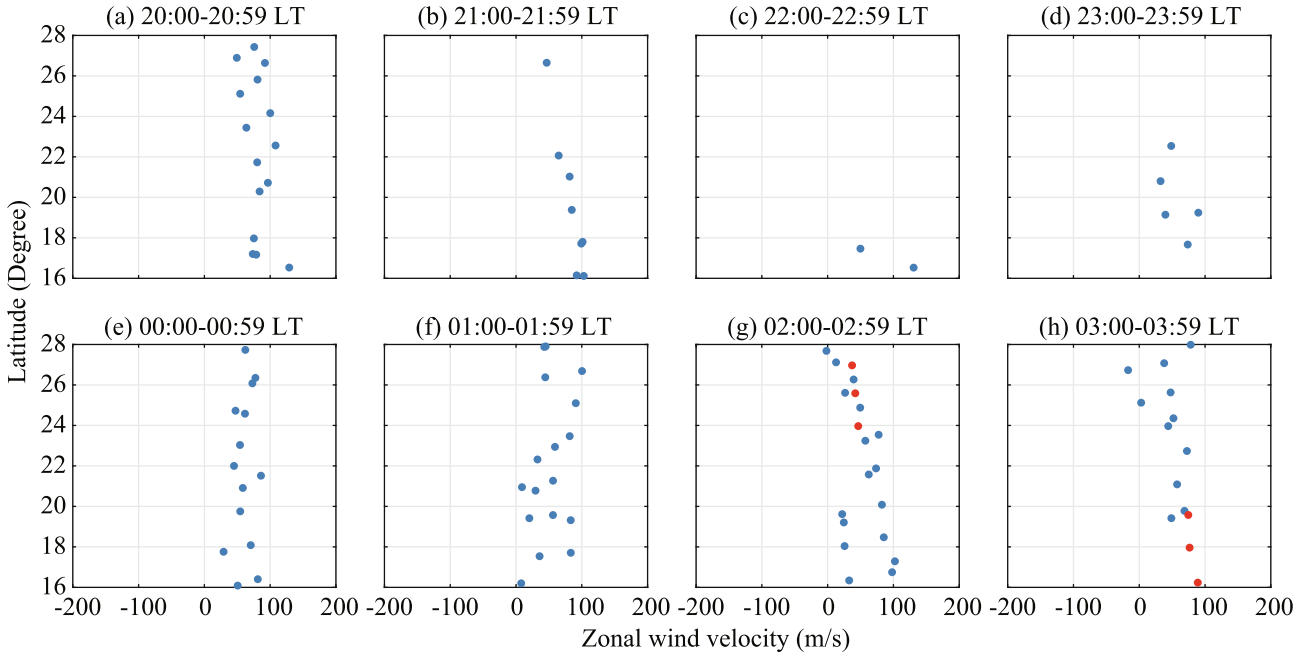

Figure 9. Averaged zonal wind velocities from 230 to 270 km at longitudes of 105°–125°E measured by MIGHTI from ICON (eastward is positive). The blue dots represent zonal wind velocities detected from March 14 to April 23, 2022 (40 days centered on April 3). The zonal wind velocity data during the night of April 3 are marked by red dots.

event, the SYM-H index was approximately −11 nT, and the Kp index was less than 3, indicating relatively quiet geomagnetic activity (Fig. 2). Note that the AE index increased from 15 to 18 UT on April 3 (22:34–02:34 LT on April 3–4) and reached a maximum at approximately 17:30 UT on April 3 (01:04 LT on April 4). This period is in accordance with the time when the EPB drift velocity increased and the poleward ends of the EPBs turned to tilt eastward. Overall, the solar and geomagnetic activity was moderate during the tilt change, but there were still some disturbances in the ionosphere caused by the geomagnetic substorm, which may have caused some small-scale zonal wind and electric field variations related to the changes in tilt directions during the night of April 3, 2022.

Previous studies have shown that the EPB drift velocity is in good agreement with the plasma drift velocity and zonal wind velocity (Chapagain et al., 2012a, 2013; Rishbeth, 1971). The main driving force of zonal plasma drifts is the zonal wind and weighted Pedersen conductivity (Eccles, 1998). In the F region of the ionosphere, zonal wind drives vertical Pedersen currents and results in a downward polarization electric field. This downward electric field couples with the magnetic field to generate zonal plasma drifts. Many studies suggest that plasmas drift with a velocity similar to that of zonal wind (Chapagain et al., 2012a; Haerendel et al., 1992; Richmond et al., 1992; Rishbeth, 1971). Chapagain et al. (2013) compared the observational data of nighttime thermospheric zonal neutral winds, EPB drift velocities, and zonal plasma drifts. These three elements are well correlated, especially after midnight, which means that the F-region dynamo is fully activated. In this event, the Zhuhai station lacked instruments for measuring the thermospheric zonal wind and zonal plasma drift velocity. We use the ion drift velocity and zonal wind velocity data obtained from ICON to investigate the latitudinal variation in these elements. After 23 LT (15:26 UT) on April 3, westward ion drift can be observed at lower latitudes, as shown in Figure 8. The faster eastward drift of ions at higher latitudes may cause the EPB to drift eastward faster at higher latitudes and tilt eastward. The variation in the eastward ion drift velocity with latitude is the key factor influencing the change in the EPB tilt directions around and after midnight on April 3.

In this EPB event, the EPBs tilted westward after sunset. During this period, the eastward zonal wind velocity slightly decreased with latitude. The poleward ends of the EPBs were closer to the equatorial ionization anomaly (EIA) north crest (~dip 15°N), where the electron densities were greatest and the lower zonal wind velocities might be related to the greater ion drag forces at higher latitudes near the EIA crest (Raghavarao et al., 1991; Martinis et al., 2001; Karan et al., 2023). As a result, the poleward ends of the EPBs drifted more slowly eastward and tilted westward after sunset during this EPB event. However, this mechanism cannot explain the eastward tilts after midnight. In addition, the zonal wind velocity calculated by the horizontal wind model decreased from 20 LT on April 3, with a maximum of 75 m/s (Fig. 5b). The zonal wind velocity from HWM14 was consistent with the EPB drift velocity before midnight, while the EPB drift velocity increased and was much greater after midnight. In fact, the wind velocity from HWM14 may not represent the actual wind velocity. The increase in the EPB drift velocity shown in Figure 5b after midnight may be related to the secondary peak of zonal wind (Chapagain et al., 2012a). When the eastward plasma drift is close to the zonal wind velocity due to the F-region dynamo, the ion drag force is negligible and causes the zonal wind to increase (Eccles, 1998; Martinis et al., 2003). Apart from the increase in the EPB drift velocity mentioned above, we should pay attention to differences in

the EPB velocity at different latitudes (colored solid lines/dashed lines for higher/lower latitudes in Fig. 5b).

For the eastward tilts of the EPBs, the altitude/latitude shear of the EPB drift velocity can be important. When the westward zonal wind in the E region is strong enough to dominate the electric field, it may generate a westward plasma drift or a slower eastward drift at lower altitudes/latitudes through the electric field and cause an eastward tilt (Huba et al., 2009; Martinis et al., 2003). The contribution of the E region can be important early at night from 20:00 to 22:30 LT (Martinis et al., 2003). However, the EPBs tilted eastward after midnight during 23:33–03:38 LT in this work, and the E region might have vanished because of the recombination of ions and electrons during this period (no echo was observed from 0 to 200 km on the ionograms). The dynamic process within the F layer assumes a preeminent and guiding role in the change in tilt. In addition, although the ion drift velocity was obviously stronger at higher latitudes, the velocity latitudinal pattern of the zonal wind almost did not change with local time in the observational results of ICON. In accordance with the formula $E = \frac{\Sigma_F^P}{\Sigma_E^P + \Sigma_F^P}(U_F \times B)$ (Heelis, 2004), larger $E \times B$ drift velocities at higher latitudes/altitudes associated with eastward tilt should correspond to greater zonal wind velocities. Assuming that the wind velocity gradient is small, the gradient of Pedersen conductivity Σ_F^P should be considered. In a two-dimensional numerical simulation (Zalesak et al., 1982), bubbles drift faster at the altitude with the greatest Pedersen conductivity, although the eastward zonal wind is assumed to be uniform in altitude near the equator. The mechanisms mentioned in this paragraph indicate that greater Pedersen conductivity at higher latitudes/altitudes may cause faster eastward plasma drifts at higher latitudes, resulting in eastward tilts. Given that the eastward tilt occurred around and after midnight, the E region may contribute less to Pedersen conductivity because of the rapid decline in electron density after sunset. Conversely, the F region may contribute more to the conductivity. Wu et al. (2017) used the TIE-GCM to simulate the latitudinal variation in Pedersen conductivity to determine the conductivity distribution favorable for the formation of eastward tilt in Southeast Asia, which is similar to the field of view of the airglow images in this work. In addition, EPB drift is generally consistent with background plasma drift. In the ionospheric dynamo effect, the polarized electric field driving the plasma zonal drift is formed by the zonal wind along the magnetic flux tube and maps along the entire magnetic field line, thus affecting the plasma drift in the geomagnetic conjugate hemisphere connected by the geomagnetic field. Local plasma drift, which is faster than zonal wind, indicates the presence of an electric field source of greater strength than the F region dynamo elsewhere along the geomagnetic field line (Coley et al., 1994). In short, the eastward tilt event in this work should be related to the faster ion drift velocity at higher latitudes/altitudes. This shear of the plasma drift velocity may result from the latitudinal/altitudinal shear of the F-region Pedersen conductivity and the presence of greater zonal winds or electric fields elsewhere along the geomagnetic field line. However, further data are needed to verify this hypothesis. In addition, the changes in EPBs are small-scale variations, while the ICON data of the ion drift velocity and zonal wind velocity exhibit large-scale variation patterns. Whether the ICON data can represent the real conditions of EPB events on April 3 needs further investigation.

In summary, the changes in the EPB tilt directions may be the result of the coupling of zonal wind, the electric field, and Pedersen conductivity variations with altitude/latitude along the geomagnetic field line.

5 Conclusions

This study investigates a notable EPB event observed during the night of April 3, 2022, characterized by significant morphological changes and associated ionospheric phenomena. The key findings are presented as follows:

1. EPB Tilt Direction and Duration: The westward-tilt EPBs changed to tilt eastward at approximately 23:27 LT in less than 17 min; tilt angles ranged from −12° to 25°. The eastward tilt lasted for nearly four hours. The drift velocities of the EPBs at relatively high latitudes clearly increased and were greater than those at lower latitudes when the EPBs turned to tilt eastward at approximately 23:27 LT (15:53 UT) on April 3, 2022.
2. Ionospheric Manifestations: Ionograms obtained from 22:34 LT to 03:14 LT during the night of April 3 demonstrated the occurrence of Spread F induced by EPBs at altitudes ranging from 300 to 400 km. Besides, the irregular electron density distributions induced by EPBs caused significant signal scintillation according to the S4 index during the night.
3. Latitudinal Variations in Drift Velocities: When the EPBs tilted eastward, the drift velocities at higher latitudes were faster than those at lower latitudes, with a velocity differential of 20 m/s. During this time period, ion drift velocities were also faster at higher latitudes. This latitudinal shear in ion drift velocity might cause the changes in the EPB tilt directions.
4. Potential Mechanisms for EPB Tilt variation: The latitudinal shear of the ion drift velocity is likely associated with the latitudinal and altitudinal gradients in the F-region Pedersen conductivity. Additionally, the presence of stronger zonal winds or electric fields along the geomagnetic field line could have contributed to these dynamics.

Acknowledgments

We are grateful to the ICON Science Data Center, HWM14 model's teams, and NASA/GSFC's Space Physics Data Facility's OMNIWeb service and OMNI data. The editor thanks two anonymous reviewers for their assistance in evaluating this paper.

Funding

This work was supported by the Project of Stable Support for Youth Team in Basic Research Field, CAS (YSBR-018); the National Natural Science Foundation of China (42188101, 42374181, 42374186, 42441814, 42274195, 42004136, 42104169, and 42104147); the Guangdong Basic and Applied Basic Research Foundation (2021A1515011216, 2022A1515011580, and 2020A1515110242); Key Innovation Team of China Meteorological Administration "Space

Weather Monitoring and Alerting" (CMA2024ZD01); "Ionospheric Forecast and Alerting Youth Innovation Team" (CMA2024QN09); the USTC Research Funds of the Double First-Class Initiative (YD2080002013); the Key Laboratory of Tropical Atmosphere-Ocean System (Sun Yat-sen University); the Ministry of Education; the Fundamental Research Funds for the Central Universities; the Opening Funding of the Chinese Academy of Sciences dedicated to the Chinese Meridian Project; and the Open Research Project of Large Research Infrastructures of CAS, "Study on the interaction between low/mid-latitude atmosphere and ionosphere based on the Chinese Meridian Project".

Data availability statement

The ICON data can be accessed at the ICON Science Data Center at the University of California, Berkeley (https://icon.ssl.berkeley.edu/Data/Data-Product-Matrix). The solar and geomagnetic indices can be accessed in the GSFC/SPDF OMNIWeb database (https://omniweb.gsfc.nasa.gov/). The airglow and digisonde data used and/or analyzed during the current study are available in the Zenodo database at doi: https://doi.org/10.5281/zenodo.11180799 (Zhong & Song, 2024).

References

Aa E, Zou S, Eastes R, Karan DK, Zhang SR, Erickson PJ, Coster AJ. 2020. Coordinated ground-based and space-based observations of equatorial plasma bubbles. *J Geophys Res Space Phys* **125(1)**: e2019ja027569. https://doi.org/10.1029/2019ja027569.

Aggson TL, Maynard NC, Herrero FA, Mayr HG, Brace LH, Liebrecht MC. 1987. Geomagnetic equatorial anomaly in zonal plasma flow. *J Geophys Res Space Phys* **92(A1)**: 311–315. https://doi.org/10.1029/JA092iA01p00311.

Anderson DN, Mendillo M. 1983. Ionospheric conditions affecting the evolution of equatorial plasma depletions. *Geophys Res Lett* **10(7)**: 541–544. https://doi.org/10.1029/GL010i007p00541.

Arruda DCS, Sobral JHA, Abdu MA, Castilho MV, Takahashi H, Medeiros AF, Buriti RA. 2006. Theoretical and experimental zonal drift velocities of the ionospheric plasma bubbles over the Brazilian region. *Adv Space Res* **38(11)**: 2610–2614. https://doi.org/10.1016/j.asr.2006.05.015.

Booker HG, Wells HW. 1938. Scattering of radio waves by the F-region of the ionosphere. *Terr Magn Atmos Electr* **43(3)**: 249–256. https://doi.org/10.1029/TE043i003p00249.

Booker HG, Wells HW. 1938. Scattering of radio waves by the F-region of the ionosphere. *Terr Magn Atmos Electr* **43(3)**: 249–256. https://doi.org/10.1029/TE043i003p00249.

Bowman GG. 1991. Ionospheric frequency spread and its relationship with range spread in mid-latitude regions. *J Geophys Res Space Phys* **A96(A6)**: 9745–9753. https://doi.org/10.1029/91JA00389.

Cai X, Burns AG, Wang W, Coster A, Qian L, Liu J, Solomon SC, Eastes RW, Daniell RE, McClintock WE. 2020. Comparison of GOLD nighttime measurements with total electron content: preliminary results. *J Geophys Res Space Phys* **125(9)**: e2019JA027767. https://doi.org/10.1029/2019JA027767.

Calabia A, Imtiaz N, Altadill D, Yasyukevich Y, Segarra A, Prol FS, Adhikari B, del Peral L, Rodriguez Frias MD, Molina I. 2024. Uncovering the drivers of responsive ionospheric dynamics to severe space weather conditions: a coordinated multi-instrumental approach. *J Geophys Res Space Phys* **129(3)**: e2023JA031862. https://doi.org/10.1029/2023JA031862.

Carrasco AJ, Pimenta AA, Wrasse CM, Batista IS, Takahashi H. 2020. Why do equatorial plasma bubbles bifurcate? *J Geophys Res Space Phys* **125(11)**: e2020JA028609. https://doi.org/10.1029/2020JA028609.

Chapagain NP, Fisher DJ, Meriwether JW, Chau JL, Makela JJ. 2013. Comparison of zonal neutral winds with equatorial plasma bubble and plasma drift velocities. *J Geophys Res Space Phys* **118(4)**: 1802–1812. https://doi.org/10.1002/jgra.50238.

Chapagain NP, Makela JJ, Meriwether JW, Fisher DJ, Buriti RA, Medeiros AF. 2012a. Comparison of nighttime zonal neutral winds and equatorial plasma bubble drift velocities over Brazil. *J Geophys Res Space Phys* **117**: A06309. https://doi.org/10.1029/2012ja017620.

Chapagain NP, Taylor MJ, Makela JJ, Duly TM. 2012b. Thermosphere ionosphere mesosphere energetics and dynamics. *J Geophys Res Space Phys* **117(A6)**: A06316. https://doi.org/10.1029/2012JA017750.

Chen G, Zhang M, Yan C, Zhang Q, Yang G, Li Y, Zhang S, Gong W, He Z. 2023. Downward drifting F-region irregularity observed above an eastward drifting one before midnight on 4 March 2014. *J Geophys Res Space Phys* **128(2)**: e2022JA031008. https://doi.org/10.1029/2022JA031008.

Coley WR, Heelis RA, Spencer NW. 1994. Comparison of low-latitude ion and neutral zonal drifts using DE 2 data. *J Geophys Res Space Phys* **99(A1)**: 341–348. https://doi.org/10.1029/93JA02205.

Das SK, Pavanchaitanya P, Patra AK, Niranjan K. 2022. On the onset time and background ionospheric conditions of postsunset equatorial plasma bubble. *J Geophys Res Space Phys* **127(12)**: e2022JA030731. https://doi.org/10.1029/2022JA030731.

Drob DP, Emmert JT, Meriwether JW, Makela JJ, Doornbos E, et al. 2015. An update to the Horizontal Wind Model (HWM): the quiet time thermosphere. *Earth Space Sci* **2(7)**: 301–319. https://doi.org/10.1002/2014EA000089.

Dungey JW. 1956. Convective diffusion in the equatorial F region. *J Atmos Terr Phys* **9(5–6)**: 304–310. https://doi.org/10.1016/0021-9169(56)90148-9.

Eccles JV. 1998. A simple model of low-latitude electric fields. *J Geophys Res Space Phys* **103(A11)**: 26699–26708. https://doi.org/10.1029/98JA02657.

Englert CR, Harlander JM, Brown CM, Marr KD, Miller IJ, et al. 2017. Michelson interferometer for global high-resolution thermospheric imaging (MIGHTI): instrument design and calibration. *Space Sci Rev* **212(1–2)**: 553–584. https://doi.org/10.1007/s11214-017-0358-4.

Greenacre M, Groenen PJF, Hastie T, D'Enza AI, Markos A, Tuzhilina E. 2022. Principal component analysis. *Nat Rev Methods Primers* **2(1)**: 100. https://doi.org/10.1038/s43586-022-00184-w.

Haerendel G, Eccles JV, Çakir S. 1992. Theory for modeling the equatorial evening ionosphere and the origin of the shear in the horizontal plasma flow. *J Geophys Res Space Phys* **97(A2)**: 1209–1223. https://doi.org/10.1029/91JA02226.

Han H, Zhong J, Hao Y, Wang N, Wan X, et al. 2024. Effects of equatorial plasma bubbles on multi-GNSS signals: a case study over South China. *Remote Sens* **16(8)**: 1358. https://doi.org/10.3390/rs16081358.

Heelis RA, Stoneback RA, Perdue MD, Depew MD, Morgan WA, Mankey MW, Lippincott CR, Harmon LL, Holt BJ. 2017. Ion velocity measurements for the ionospheric connections explorer. *Space Sci Rev* **212(1–2)**: 615–629. https://doi.org/10.1007/s11214-017-0383-3.

Heelis RA. 2004. Electrodynamics in the low and middle latitude ionosphere: a tutorial. *J Atmos Sol Terr Phys* **66(10)**: 825–838. https://doi.org/10.1016/j.jastp.2004.01.034.

Huba JD, Ossakow SL, Joyce G, Krall J, England SL. 2009. Three-dimensional equatorial spread F modeling: Zonal neutral wind effects. *Geophys Res Lett* **36(19)**: L19106. https://doi.org/10.1029/2009GL040284.

Immel TJ, England SL, Mende SB, Heelis RA, Englert CR, et al. 2018. The ionospheric connection explorer mission: mission goals and design. *Space Sci Rev* **214(1)**: 13. https://doi.org/10.1007/s11214-017-0449-2.

Karan DK, Eastes RW, Martinis CR, Daniell RE, Solomon SC, McClintock WE. 2023. Unique combinations of differently shaped equatorial plasma bubbles occurring within a small longitude range. *J Geophys Res Space Phys* **128(11)**: e2023JA031625. https://doi.org/10.1029/2023JA031625.

Kelley MC, Makela JJ, Paxton LJ, Kamalabadi F, Comberiate JM, Kil H. 2003. The first coordinated ground- and space-based optical observations of equatorial plasma bubbles. *Geophys Res Lett* **30(14)**: 1766. https://doi.org/10.1029/2003gl017301.

Kil H, Heelis RA, Paxton LJ, Oh S-J. 2009. Formation of a plasma depletion shell in the equatorial ionosphere. *J Geophys Res Space Phys* **114(A11)**: A11302. https://doi.org/10.1029/2009JA014369.

Kil H, Su S-Y, Paxton LJ, Wolven BC, Zhang Y, Morrison D, Yeh HC. 2004. Coincident equatorial bubble detection by TIMED/GUVI and ROCSAT-1. *Geophys Res Lett* **31(3)**: L03809. https://doi.org/10.1029/2003GL018696.

King GAM. 1970. Spread-F on ionograms. *J Atmos Terr Phys* **32(2)**: 209–221. https://doi.org/10.1016/0021-9169(70)90192-3.

Magdaleno S, Herraiz M, Altadill D, de la Morena BA. 2017. Climatology characterization of equatorial plasma bubbles using GPS data. *J. Space Weather Space Clim* **7(A3)**: 12. https://doi.org/10.1051/swsc/2016039.

Martinis C, Eccles JV, Baumgardner J, Manzano J, Mendillo M. 2003. Latitude dependence of zonal plasma drifts obtained from dual-site airglow observations. *J Geophys Res Space Phys* **108(3)**: 1129. https://doi.org/10.1029/2002JA009462.

Martinis C, Meriwether J, Niciejewski R, Biondi M, Fesen C, Mendillo M. 2001. Zonal neutral winds at equatorial and low latitudes. *J Atmos Sol Terr Phys* **63(14)**: 1559–1569. https://doi.org/10.1016/s1364-6826(01)00022-0.

Miller ES, Makela JJ, Groves KM, Kelley MC, Tsunoda RT. 2010. Coordinated study of coherent radar backscatter and optical airglow depletions in the central Pacific. *J Geophys Res Space Phys* **115(6)**: A06307. https://doi.org/10.1029/2009JA014946.

Ossakow SL, Zalesak ST, McDonald BE, Chaturvedi PK. 1979. Nonlinear equatorial spread F: Dependence on altitude of the F peak and bottomside background electron density gradient scale length. *J Geophys Res Space Phys* **84(A1)**: 17–29. https://doi.org/10.1029/JA084iA01p00017.

Otsu N. 1979. A threshold selection method from gray-level histograms. *IEEE Trans Syst Man Cybern* **9(1)**: 62–66. https://doi.org/10.1109/TSMC.1979.4310076.

Otsuka Y, Shiokawa K, Ogawa T, Yokoyama T, Yamamoto M, Fukao S. 2004. Spatial relationship of equatorial plasma bubbles and field-aligned irregularities observed with an all-sky airglow imager and the equatorial atmosphere radar. *Geophys Res Lett* **31(20)**: L20802. https://doi.org/10.1029/2004gl020869.

Otsuka Y, Shiokawa K, Ogawa T, Wilkinson P. 2002. Geomagnetic conjugate observations of equatorial airglow depletions. *Geophys Res Lett* **29(15)**: 1753. https://doi.org/10.1029/2002gl015347.

Pearson K. 1901. LIII. On lines and planes of closest fit to systems of points in space. *Lond Edinb Dubl Phil Mag J Sci* **2(11)**: 559–572. https://doi.org/10.1080/14786440109462720.

Raghavarao R, Wharton LE, Spencer NW, Mayr HG, Brace LH. 1991. An equatorial temperature and wind anomaly (ETWA). *Geophys Res Lett* **18(7)**: 1193–1196. https://doi.org/10.1029/91GL01561.

Richmond AD, Ridley EC, Roble RG. 1992. A thermosphere/ionosphere general circulation model with coupled electrodynamics. *Geophys Res Lett* **19(6)**: 601–604. https://doi.org/10.1029/92GL00401.

Richmond AD, Fang T-W, Maute A. 2015. Electrodynamics of the equatorial evening ionosphere: 1. Importance of winds in different regions. *J Geophys Res Space Phys* **120(3)**: 2118–2132. https://doi.org/10.1002/2014JA020934.

Rishbeth H. 1971. Polarization fields produced by winds in the equatorial F-region., *Planet Space Sci* **19(3)**: 357–369. https://doi.org/10.1016/0032-0633(71)90098-5.

Sinha HSS, Raizada S. 2000. Some new features of ionospheric plasma depletions over the Indian zone using all sky optical imaging. *Earth Planet Space* **52(8)**: 549–559. https://doi.org/10.1186/bf03351662.

Sultan PJ. 1996. Linear theory and modeling of the Rayleigh-Taylor instability leading to the occurrence of equatorial spread F. *J Geophys Res Space Phys* **101(A12)**: 26875–26891. https://doi.org/10.1029/96ja00682.

Sun L, Xu J, Zhu Y, Yuan W, Zhao X. 2021. Case study of an Equatorial plasma bubble event investigated by multiple ground-based instruments at low latitudes over China. *Earth Planet Phys* **5(5)**: 435–449. https://doi.org/10.26464/epp2021048.

Sun L , Xu J, Wang W, Yuan W, Li Q, Jiang C. 2016. A statistical analysis of equatorial plasma bubble structures based on an all-sky airglow imager network in China. *J Geophys Res Space Phys* **121(11)**: 11495–11517. https://doi.org/10.1002/2016ja022950.

Tsunoda RT, White BR. 1981. On the generation and growth of equatorial backscatter plumes 1. Wave structure in the bottomside F layer. *J Geophys Res Space Phys* **86(A5)**: 3610–3616. https://doi.org/10.1029/JA086iA05p03610.

Vital LFR, Takahashi H , Barros D, Carmo CS, Carrasco AJ, Wrasse CM, Figueiredo CAOB. 2024. Seasonal and solar cycle dependency of relationship between equatorial plasma bubbles and Rayleigh-Taylor instability growth rate. *Space Weather* **22(10)**, e2024SW003959. https://doi.org/10.1029/2024SW003959.

Wang GJ, Shi JK, Reinisch BW, Wang X, Wang Z 2015. Ionospheric plasma bubbles observed concurrently by multi-instruments over low-latitude station Hainan. *J Geophys Res Space Phys* **120(3)**: 2288–2298. https://doi.org/10.1002/2014JA020245.

Weber EJ, Buchau J, Eather RH , Mende SB. 1978. North-south aligned equatorial airglow depletions. *J Geophys Res Space Phys* **83(A2)**: 712–716. https://doi.org/10.1029/JA083iA02p00712.

Woodman RF, La Hoz C. 1976. Radar observations of F region equatorial irregularities. *J Geophys Res* **81(31)**: 5447–5466. https://doi.org/10.1029/JA081i031p05447.

Woodman RF. 2009. Spread F – an old equatorial aeronomy problem finally resolved? *Ann Geophys* **27(5)**: 1915–1934. https://doi.org/10.5194/angeo-27-1915-2009.

Wu K, Xu J, Wang W, Sun L, Liu X, Yuan W. 2017. Interesting equatorial plasma bubbles observed by all-sky imagers in the equatorial region of China. *J Geophys Res Space Phys* **122(10)**: 10596–10611. https://doi.org/10.1002/2017JA024561.

Wu K, Xu J, Zhu Y, Yuan W. 2021. Ionospheric plasma vertical drift and zonal wind variations cause unusual evolution of EPBs during a geomagnetically quiet night. *J Geophys Res Space Phys* **126(12)**: e2021ja029893. https://doi.org/10.1029/2021ja029893.

Xiong C, Xu J, Wu K, Yuan W. 2018a. Longitudinal thin structure of equatorial plasma depletions coincidently observed by swarm

constellation and all-sky imager. *J Geophys Res Space Phys* **123(2)**: 1593–1602. https://doi.org/10.1002/2017JA025091.

Xiong C, Stolle C, Park J. 2018b. Climatology of GPS signal loss observed by Swarm satellites. *Ann Geophys* **36**: 679–693. https://doi.org/10.5194/angeo-36-679-2018.

Yao M, Chen G, Zhao ZY, Wang YH, Bai B. 2012. A novel low-power multifunctional ionospheric sounding system. *IEEE Trans Instrum Meas* **61(5)**: 1252–1259. https://doi.org/10.1109/tim.2011.2174903.

Yokoyama T, Shinagawa H, Jin H. 2014. Nonlinear growth, bifurcation, and pinching of equatorial plasma bubble simulated by three-dimensional high-resolution bubble model. *J Geophys Res Space Phys* **119(12)**: 10474–10482. https://doi.org/10.1002/2014ja020708.

Zakharenkova I, Cherniak I, Braun JJ, Wu Q. 2023. Global maps of equatorial plasma bubbles depletions based on FORMOSAT-7/COSMIC-2 ion velocity meter plasma density observations. *Space Weather* **21(5)**: e2023SW003438. https://doi.org/10.1029/2023SW003438.

Zalesak ST, Ossakow SL, Chaturvedi PK. 1982. Nonlinear equatorial spread F: The effect of neutral winds and background Pedersen conductivity. *J Geophys Res Space Phys* **87(A1)**: 151–166. https://doi.org/10.1029/JA087iA01p00151.

Zhong J, Song X. 2024. *Datasets for airglow image data and ionogram data obtained from Zhuhai Station (113.58°E, 22.35°N) on April 3, 2022* [Data set]. Zenodo. https://doi.org/10.5281/zenodo.11180799.

Zou KH, Tuncali K, Silverman SG. 2003. Correlation and simple linear regression. *Radiology* **227(3)**: 617–628. https://doi.org/10.1148/radiol.2273011499.

Cite this article as: Song X, Zhong J, Hao Y, Bai T, Wan X, et al. 2025. Transition from westward to eastward tilts of equatorial plasma bubbles observed by an all-sky airglow imager. *J. Space Weather Space Clim.* **15**, 38. https://doi.org/10.1051/swsc/2025032.